Rare Metal Materials and Engineering
Volume 51, Issue 9, September 2022
Available online at www.rmme.ac.cn

Science Press

Cite this article as: Song Fei, Wang Ning, Su Nan, et al. Numerical Simulation of Hot Stamping Process for Saddle Shape Part of TA32 Titanium Alloy[J]. Rare Metal Materials and Engineering, 2022, 51(09): 3252-3262.

ARTICLE

Numerical Simulation of Hot Stamping Process for Saddle Shape Part of TA32 Titanium Alloy

Song Fei, Wang Ning, Su Nan, Chen Minghe, Xie Lansheng

National Key Laboratory of Science and Technology on Helicopter Transmission, Nanjing University of Aeronautics and Astronautics, Nanjing 210016, China

Abstract: The constitutive model of TA32 titanium alloy was established, and different drawbeads were added on the die to eliminate the wrinkles. The Barlat 89 and Hill 48 yield criterions were used to compare the prediction accuracy of the finite element simulations. The saddle shape part of TA32 titanium alloy was hot-stamped, and the thickness distribution was measured and compared with the simulation results. Results show that the wrinkles can be effectively eliminated by adding the drawbeads along *X*-axis and *Y*-axis. The saddle shape part can be precisely formed without defects. The finite element model with Barlat 89 yield criterion has better prediction accuracy than that with Hill 48 yield criterion does, indicating that the finite element simulation has good theoretical prediction significance. The mechanical properties and microstructure of the hot-stamped part were investigated and it is found that they all meet the practical engineering requirements.

Key words: TA32 titanium alloy; hot stamping; saddle shape part; finite element simulation; drawbeads; yield criterion

Over the decades, titanium and titanium alloy products have been extensively used in aerospace, marine, and automotive industries due to their excellent properties, such as low density, high strength, good corrosion resistance, and great creep resistance[1,2]. TA32 titanium alloy is a near-α high-temperature titanium alloy with superior mechanical properties and creep resistance at elevated temperatures. Therefore, the mechanical properties and microstructure evolution at high temperatures of TA32 titanium alloy have been widely studied due to the urgent requirements of lightweight design at high service temperature in aero engine[3-5]. However, the engineering application of TA32 titanium alloy is still restricted. Owing to the poor ductility of TA32 alloy at room temperature, the hot stamping is commonly used to improve its formability[6,7]. Consequently, the forming limit stress diagram (FLSD) is adopted to evaluate the formability[8]. At elevated temperatures, the elongation is largely increased, thereby reducing the fracture risk. In addition, the springback can be effectively suppressed when the flow stress drops and the stress relaxation is enhanced[9]. To meet the manufacture requirements of complex engine exhaust pipe parts of TA32 titanium alloy, it is of great importance to conduct the finite element simulations and experiments about the hot stamping forming process.

In this study, the saddle shape part with double-curvature profile was investigated, as shown in Fig.1. There is a strong wrinkling tendency at the center of the saddle shape part, which is difficult to eliminate, especially when the saddle shape part is treated by step stamping. Adding drawbeads and blank holders is effective to prevent the wrinkling[10,11]. Usually, the drawbeads are placed on the blank holder, and the drawing force can be adjusted by the drawbead shape, blank holder force, and friction coefficient[12-14]. However, the further investigations of the drawbeads on punch and die during hot stamping are rarely reported. Therefore, the optimal drawbead design for wrinkle elimination is necessary.

The material model and applied yield criterion are important factors affecting the accuracy of the numerical simulation. The Arrhenius and Johnson-Cook constitutive models can provide precise prediction for the flow stress at elevated temperatures of titanium alloy[15,16]. The Hill 1948, Barlat 1989, Barlat 1996, Barlat 2000, and Cazacu Barlat

Received date: September 03, 2021
Foundation item: Aviation Key Fund Project of China (20153021001)
Corresponding author: Chen Minghe, Ph. D., Professor, National Key Laboratory of Science and Technology on Helicopter Transmission, Nanjing University of Aeronautics and Astronautics, Nanjing 210016, P. R. China, E-mail: meemhchen@nuaa.edu.cn

anisotropic yield criteria have been used in numerical investigation for warm deep drawing of Ti-6Al-4V alloy at 400 °C[17-19]. Different anisotropic yield criteria (Barlat 1989, Barlat 1996, Hill 1993) and different hardening models are used to predict FLSDs of Ti-6Al-4V alloy under warm conditions[20].

In this research, the influence of drawbeads on wrinkle suppression during the hot stamping of the TA32 alloy saddle shape part was investigated. The Barlat 89 and Hill 48 yield criteria were used for the numerical simulation, and the simulated results were compared with the experimental ones to verify the prediction accuracy. This research provides guidance for the parameter design of the hot stamping process for TA32 titanium alloy.

1 Materials and Anisotropic Yield Criterion

TA32 alloy is a near-α high temperature titanium alloy, and its β phase transition temperature is 1000±10 °C[21]. The thickness of TA32 alloy sheet was 0.8 mm, and its nominal chemical composition is listed in Table 1.

The developed Arrhenius constitutive model[22] is as follows:

$$\sigma = \frac{1}{\alpha}\ln\left\{\left(\frac{Z}{A}\right)^{\frac{1}{n}} + \left[\left(\frac{Z}{A}\right)^{\frac{2}{n}} + 1\right]^{\frac{1}{2}}\right\} \quad (1)$$

$$Z = \dot{\varepsilon}\exp\left(\frac{-Q}{R_g T}\right) \quad (2)$$

$$\alpha = 0.0233\varepsilon^4 + 0.0433\varepsilon^3 + 0.0423\varepsilon^2 - 0.0423\varepsilon + 0.0122 \quad (3)$$

$$n = 0.0270\varepsilon^4 + 0.0758\varepsilon^3 + 0.0219\varepsilon^2 + 0.6683\varepsilon + 2.4884 \quad (4)$$

$$Q = -8.67\varepsilon^5 - 1.866\varepsilon^4 - 5.284\varepsilon^3 - 12.067\varepsilon^2 - 15.233\varepsilon + 30.516 \quad (5)$$

$$\ln A = -0.583\varepsilon^5 - 1.866\varepsilon^4 - 5.284\varepsilon^3 - 12.067\varepsilon^2 - 15.233\varepsilon + 30.516 \quad (6)$$

where σ is the flow stress (MPa); ε is the strain; $\dot{\varepsilon}$ is the strain rate (s^{-1}); T is the absolute temperature (K); Q is the activation energy (kJ·mol^{-1}); α, A, and Z are the material constants; R_g is the universal gas constant (8.314 J·mol^{-1}·K^{-1}). Thus, the flow stress is a function of the strain, strain rate, and temperature. In this study, the hot stamping was conducted at 800 °C. The true stress-strain curves of TA32 alloy at 800 °C were obtained by uniaxial tensile tests. The experimental true stress-true strain curves are shown in Fig.2.

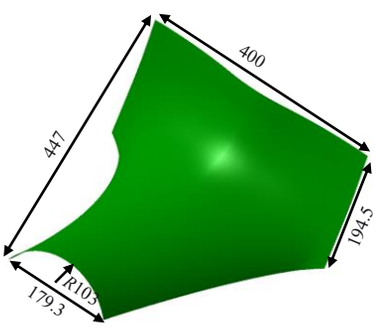

Fig.1 Schematic diagram of saddle shape part of TA32 alloy

Table 1 Chemical composition of TA32 titanium alloy (wt%)

Al	Sn	Zr	Mo	Si	Nb	Ta	Ti
5.5	3.5	3.0	0.7	0.3	0.4	0.4	Bal.

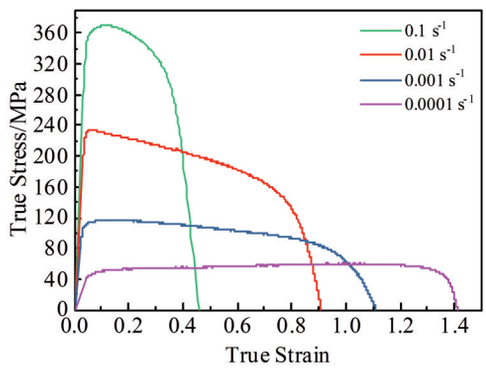

Fig.2 Experimental true stress-true strain curves of TA32 alloys at 800 °C

2 Finite Element Analysis

2.1 Finite element model

The finite element model was established by Dynaform5.9[23]. The assembled model of blank and forming tools without drawbeads is shown in Fig. 3. The quarter symmetry model was applied in the simulation, as shown in Fig. 4. The die and punch were defined as rigid parts. The models with Barlat 89 and Hill 48 yield criteria were applied on the blank to study the effect of yield criterion on the simulation results. The friction coefficient was set as 0.05 with the boron nitride as lubricant[24]. The strain rate of 0.01 s^{-1} was applied for the finite element simulations, and the corresponding FLSD[25] is shown in Fig. 5 to predict the fracture of TA32 alloy at 800 °C.

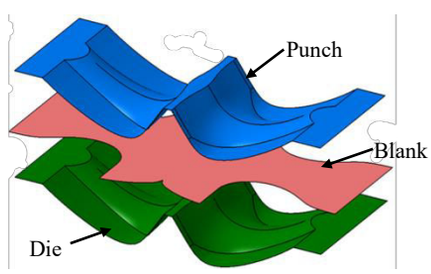

Fig.3 Assembled model of blank and forming tools without drawbeads

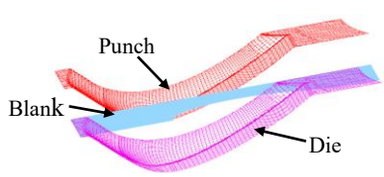

Fig.4 Schematic diagram of quarter symmetry finite element model

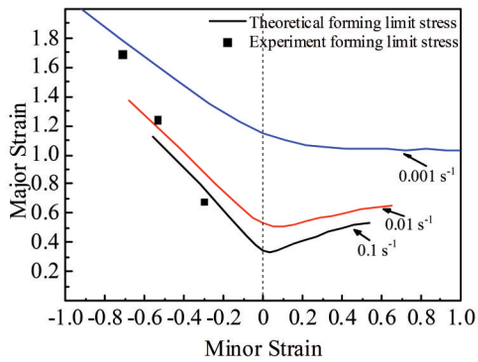

Fig.5 FLSD of TA32 alloy at 800 °C

2.2 Anisotropic yield criterion models

2.2.1 Hill 48 yield criterion

The Hill 48 yield criterion[26] has been extensively used in finite element simulation of sheet metal forming processes to describe the anisotropic behavior, which can be expressed by the quadratic function, as follows:

$$2f(\sigma_{ij}) \equiv F(\sigma_{22}-\sigma_{33})^2 + G(\sigma_{33}-\sigma_{11})^2 + H(\sigma_{11}-\sigma_{22})^2 + 2L\sigma_{23}^2 + 2M\sigma_{31}^2 + 2N\sigma_{12}^2 \quad (7)$$

where F, G, H, L, M, and N are independent constants; the subscripts 1, 2, and 3 indicate the rolling direction, transverse direction, and the normal direction, respectively. The relationship between the Lankford parameters and the independent constants can be expressed as follows:

$$\begin{cases} r_0 = \dfrac{H}{G} \\ r_{90} = \dfrac{H}{F} \\ r_{45} = \dfrac{N}{F+N} - \dfrac{1}{2} \end{cases} \quad (8)$$

where r_0, r_{45}, and r_{90} are the Lankford parameters measured by uniaxial tension along the directions with an angle of 0°, 45°, and 90° from rolling direction, respectively. At plane stress state, the Hill 48 yield criterion can be simplified as follows:

$$\begin{cases} \sigma_{11} = \sigma_1 \\ \sigma_{22} = \sigma_2 \\ \sigma_{33} = 0 \\ \sigma_{13} = 0 \\ \sigma_{23} = 0 \end{cases} \quad (9)$$

$$\begin{cases} F = \dfrac{r_0}{r_{90}(r_0+1)} \\ G = \dfrac{1}{r_0+1} \\ H = \dfrac{r_0}{r_0+1} \\ N = \dfrac{(r_0+r_{90})(1+2r_{45})}{2r_{90}(r_0+1)} \end{cases} \quad (10)$$

$$f(\sigma) = \sqrt{\sigma_1^2 - \frac{2r_0}{r_0+1}\sigma_1\sigma_2 + \frac{r_0 r_{90}+r_0}{r_{90}(1+r_0)}\sigma_2^2 + \frac{(r_0+r_{90})(1+r_{45})}{r_0(1+r_0)}\sigma_{12}^2} \quad (11)$$

2.2.2 Barlat 89 yield criterion

The Barlat 89 yield criterion[27] is also widely used in finite element simulation to describe the anisotropic behavior of the sheet metal at plane stress state, as follows:

$$\Phi = \alpha|K_1+K_2|^m + \alpha|K_1-K_2|^m + c|2K_2|^m = 2\sigma_y^m \quad (12)$$

$$K_1 = \frac{\sigma_x + h\sigma_y}{2} \quad (13)$$

$$K_2 = \sqrt{\left(\frac{\sigma_x - h\sigma_y}{2}\right)^2 + p^2\tau_{xy}^2} \quad (14)$$

$$\begin{cases} a = 2 - 2\sqrt{\dfrac{r_0}{1+r_0}\dfrac{r_{90}}{1+r_{90}}} \\ c = 2 - a \\ h = \sqrt{\dfrac{r_0}{1+r_0}\dfrac{1+r_{90}}{r_{90}}} \end{cases} \quad (15)$$

$$r_\theta = \frac{2\sigma_y^m}{\left(\dfrac{\partial\Phi}{\partial\sigma_x} + \dfrac{\partial\Phi}{\partial\sigma_y}\right)\sigma_\theta} - 1 \quad (16)$$

where Φ is the yield function; K_1 and K_2 are stress tensor invariants; m is the material constant; σ_y and σ_x are the stress along the y and x axes, respectively; r_θ is anisotropy ratio along the direction with the θ angle from rolling direction; σ_θ is the stress along the direction with the θ angle from rolling direction; τ_{xy} is shear stress; a, c, and h are the functions of anisotropy ratio; p is the anisotropy parameter. When θ=45°, the anisotropy parameter p can be obtained, as follows:

$$g(p) = \frac{2m\sigma_y^m}{\left(\dfrac{\partial\Phi}{\partial\sigma_x} + \dfrac{\partial\Phi}{\partial\sigma_y}\right)\sigma_\theta} - 1 - r_{45} \quad (17)$$

The yield loci of TA32 alloy at 800 °C with different yield criteria are shown in Fig.6. $\bar{\sigma}$ is the yield stress.

The parameters of simulation models with Barlat 89 and Hill 48 yield criteria are shown in Table 2 and Table 3, respectively.

2.3 Drawbead design and optimization

The predicted wrinkling and thickness distributions with different yield criteria are shown in Fig. 7. FLSDs with different yield criteria are shown in Fig. 8, where ε_1 is the

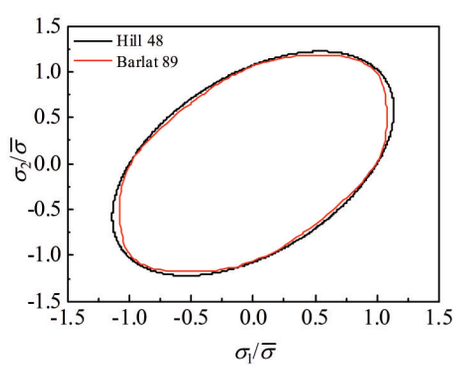

Fig.6 Yield loci of TA32 alloy at plane stress state and 800 °C with different yield criteria

Table 2 Parameters of simulation model with Barlat 89 yield criterion of TA32 alloy

Temperature/°C	Mass density/kg·m^{-3}	Young's modulus/MPa	Poisson's ratio	m	r_0	r_{45}	r_{90}
800	4 500	78 000	0.3	6	0.65	1.05	1.05

Table 3 Parameters of simulation model with Hill 48 yield criterion of TA32 alloy

Temperature/°C	Mass density/kg·m^{-3}	Young's modulus/MPa	Poisson's ratio	Yield stress/MPa	Anisotropic constant
800	4 500	78 000	0.3	187.74	0.95

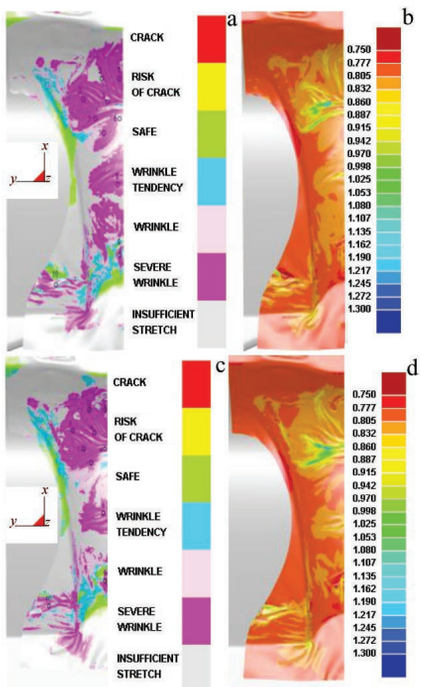

Fig.7 Predicted wrinkling (a, c) and thickness (b, d) distributions with Barlat 89 (a, b) and Hill 48 (c, d) criteria

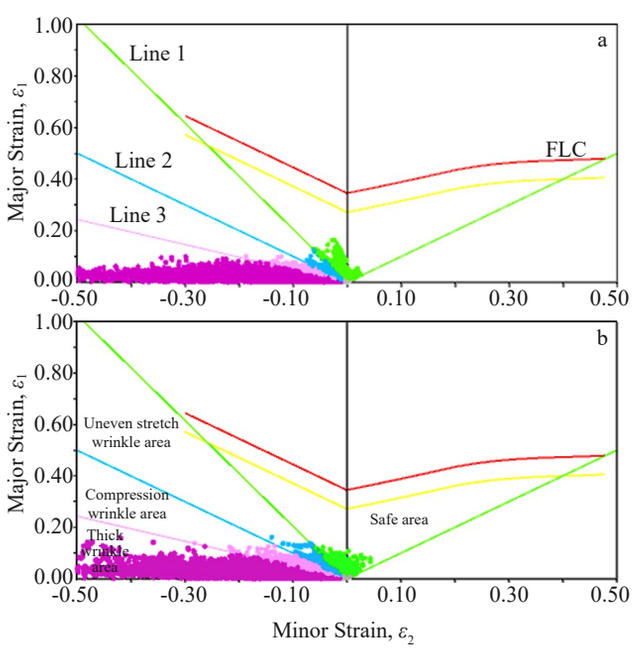

Fig.8 FLSDs with Balart 89 (a) and Hill 48 (b) yield criteria

major strain, ε_2 is the minor strain, R is the thickness anisotropy coefficient, Line 1 corresponds to the equation $\varepsilon_1+\varepsilon_2(R+1)/R=0$, Line 2 corresponds to the equation $\varepsilon_1+\varepsilon_2=0$, and Line 3 corresponds to the equation $\varepsilon_1+\varepsilon_2R/(R+1)=0$. FLC indicates the forming limit curve. There are severe wrinkles at the center of the saddle shape part, as shown in Fig.7a and 7c. The direction of wrinkles is mainly along the *Y*-axis. The predicted major strain and minor strain distributions with and without drawbeads are shown in Fig. 9, and the strains and wrinkle predictions with and without drawbeads are shown in Fig. 10. Ten points were selected for the wrinkle prediction, among which Point 1~5, 8, and 10 are in the thick wrinkle area with $\varepsilon_1+\varepsilon_2R/(R+1)<0$, Point 7 is in the compression wrinkle area with $\varepsilon_1+\varepsilon_2<0$ and $\varepsilon_1+\varepsilon_2R/(R+1)>0$, Point 6 and 9 are in the uneven stretch wrinkle area with $\varepsilon_1+\varepsilon_2(R+1)/R<0$ and $\varepsilon_1+\varepsilon_2>0$. These results suggest that the wrinkles in the saddle shape part are mainly compression wrinkles. Thus, the drawbead design is necessary for the elimination of wrinkles during the forming process.

The existence of drawbead along *Y*-axis can restrict the stress flow along *X*-axis. Three drawbeads along *Y*-axis with the optimal dimensions were applied in the simulation with Barlat 89 yield criterion. The simulation results are shown in Fig.9. It can be seen that the drawbead along *Y*-axis effectively reduces the wrinkles, and Drawbead B and C show better resistance to wrinkle formation. The predicted major strain and minor strain distributions in saddle shape part with and without different drawbeads are shown in Fig. 10. Ten points were selected to measure the strain, and the results are shown in Fig. 11. It can be found that in the saddle shape parts with Drawbead B and C, all ten points obey the constraint $\varepsilon_1+\varepsilon_2R/(R+1)>0$, indicating that no thick wrinkle exists. Point 1 and 2 are located in the compression wrinkle area with $\varepsilon_1+\varepsilon_2<0$. At Point 1~7, the strains all obey the constraint $\varepsilon_1+\varepsilon_2(R+1)/R<0$, suggesting that the areas around Point 3~7 have uneven stretch wrinkle tendency and Point 1 and 2 are located in the safe area.

In the saddle shape part with Drawbead C, most wrinkles can be eliminated. To completely eliminate the wrinkles, the drawbead along *X*-axis is added. On the basis of the application of Drawbead C, the saddle shape parts are further ameliorated by Drawbead D and E along *X*-axis under Barlat 89 yield criterion, as shown in Fig. 12a and Fig. 13a, respectively. The simulation results of saddle shape parts with different drawbeads under Barlat 89 yield criterion are shown in Fig.12 and Fig.13. It can be seen that both Drawbead D and E further improve the forming quality on the basis of saddle

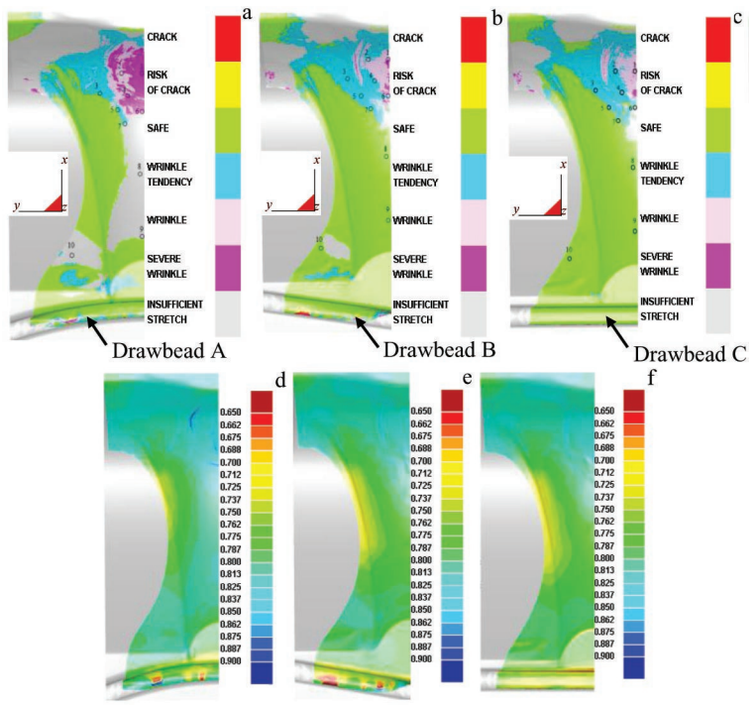

Fig.9 Predicted wrinkle (a~c) and thickness (d~f) distributions in saddle shape parts with different drawbeads under Barlat 89 yield criterion: (a, d) Drawbead A, (b, e) Drawbead B, and (c, f) Drawbead C

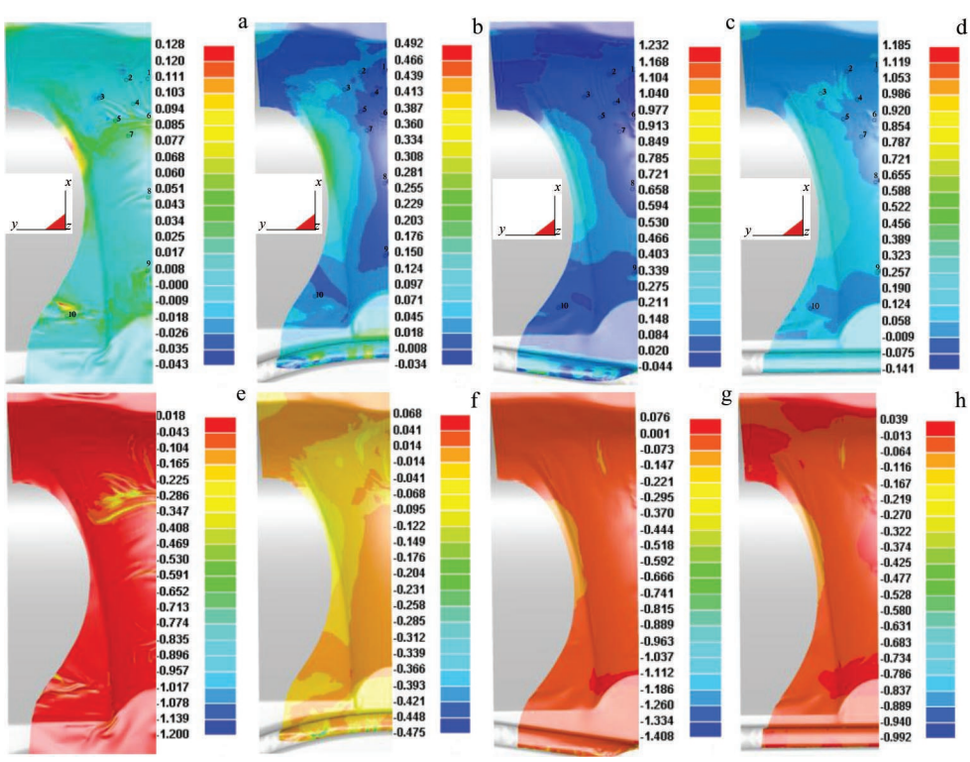

Fig.10 Predicted major strain ε_1 (a~d) and minor strain ε_2 (e~h) distributions in saddle shape parts with different drawbeads under Barlat 89 yield criterion: (a, e) without drawbead; (b, f) Drawbead A; (c, g) Drawbead B; (d, h) Drawbead C

shape part with Drawbead C. The simulation results of the major and minor strain distributions are shown in Fig. 14, and the strains at selected points are shown in Fig. 15. According to Fig. 15a, Point 2 and 4 are in the uneven stretch wrinkle area with $\varepsilon_1+\varepsilon_2>0$ and $\varepsilon_1+\varepsilon_2(R+1)/R<0$; whereas Point 8 is in the thick wrinkle area with $\varepsilon_1+\varepsilon_2R/(R+1)<0$. As shown in

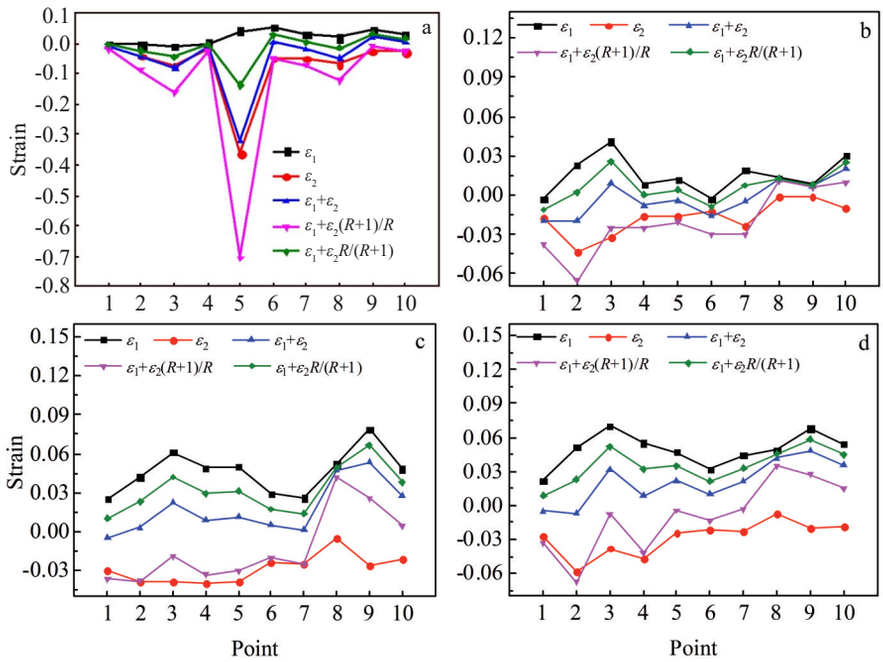

Fig.11 Strains at selected 10 points of saddle shape parts with different drawbeads under Barlat 89 yield criterion: (a) without drawbead; (b) Drawbead A; (c) Drawbead B; (d) Drawbead C

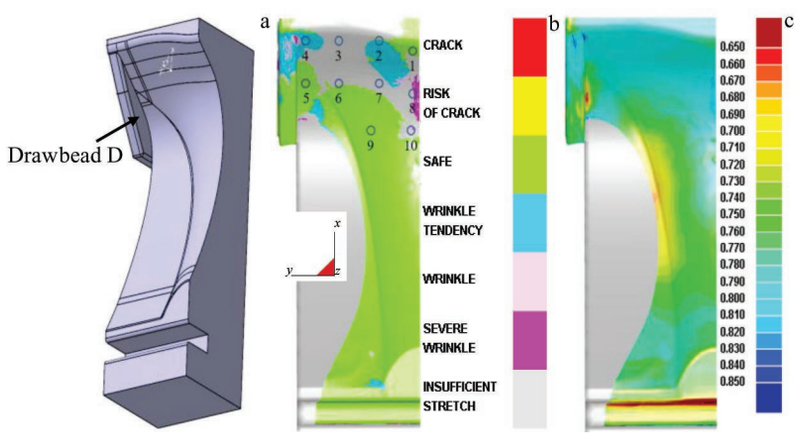

Fig.12 Schematic diagram of saddle shape part with Drawbead D (a); predicted wrinkle (b) and thickness (c) distributions of saddle shape part with Drawbead D under Barlat 89 yield criterion

Fig.15b, all points obey the constraint $\varepsilon_1+\varepsilon_2(R+1)/R>0$, indicating that all the points are in the safe area. Therefore, the Drawbead E has better resistance against the wrinkle than Drawbead D does.

The simulation results of major strain and minor strain distributions of the saddle shape part with Drawbead C and Drawbead E under Hill 48 yield criterion are shown in Fig.16. The strain measurement results of saddle shape part with Drawbead E are shown in Fig. 17. Point 2 and 3 are in the uneven stretch wrinkle area with $\varepsilon_1+\varepsilon_2>0$ and $\varepsilon_1+\varepsilon_2(R+1)/R<0$. Point 8 is in the compression wrinkle area with $\varepsilon_1+\varepsilon_2<0$. A few small wrinkles can still be observed in the saddle shape part with Drawbead E under Hill 48 yield criterion.

The simulation results show that because the drawbeads restrict the stress flow into the middle part of the saddle shape part, the stretching strain is increased while the compression strain is reduced. The wrinkles can be eliminated by adding drawbeads along *X* and *Y* directions.

3 Experiment

Based on the finite element analysis of drawbead optimization, the hot stamping tools were manufactured, as shown in Fig. 18. The forming tools were firstly heated to 800 °C. Then the TA32 alloy blank was processed into molds, held for 10 min, and finally hot-stamped. The punch speed was 5 mm/s during the forming. The hot-stamped part was placed in the closed tools for 8 min for stress relaxion, thereby reducing the springback. The heating path of the blank during

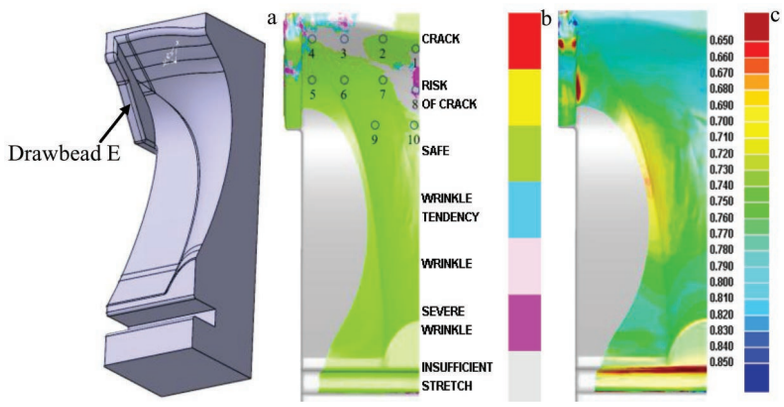

Fig.13 Schematic diagram of saddle shape part with Drawbead E (a); predicted wrinkle (b) and thickness (c) distributions of saddle shape part with Drawbead E under Barlat 89 yield criterion

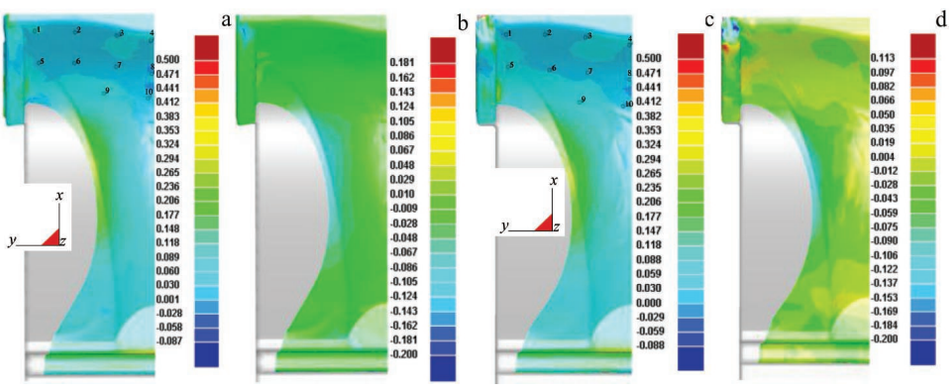

Fig.14 Predicted major strain ε_1 (a, c) and minor strain ε_2 (b, d) distributions of saddle shape parts with Drawbead D (a, b) and Drawbead E (c, d) under Barlat 89 yield criterion

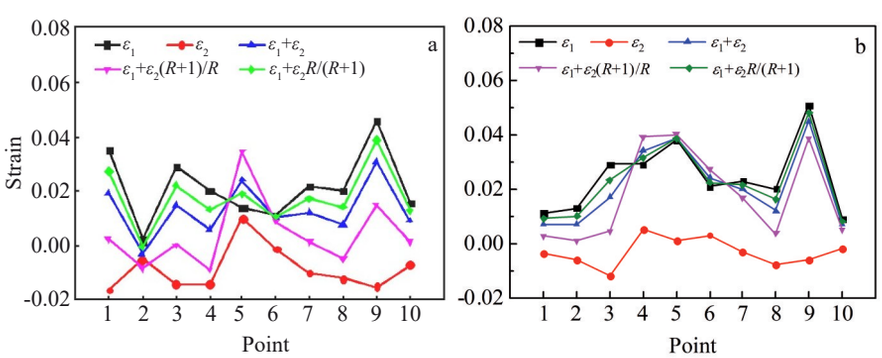

Fig.15 Strains at selected 10 points of saddle shape parts with Drawbead D (a) and Drawbead E (b) under Barlat 89 yield criterion

hot stamping is shown in Fig. 19. Fig. 18c shows the stamped saddle shape part without wrinkles, indicating that the drawbead design can effectively prevent the wrinkle of the saddle shape part during hot stamping.

4 Results and Discussion

4.1 Thickness distribution

The thickness of the formed saddle shape part at 20 points was measured by ultrasonic thickness meter and compared with the finite element simulation results, as shown in Fig.20. The maximum thickening rate R_{max}, maximum thinning rate R_{min}, average thickness T_a, thickness deviation S_d, and relative error R_c between the thicknesses measured by experiment and simulation can be calculated by Eq.(18~22), as follows:

$$R_{max} = \left|(T_{max} - T)/T\right| \times 100\% \quad (18)$$

$$T_a = \sum_{i=1}^{n} T_i/n \quad (19)$$

$$R_{min} = \left|(T_{min} - T)/T\right| \times 100\% \quad (20)$$

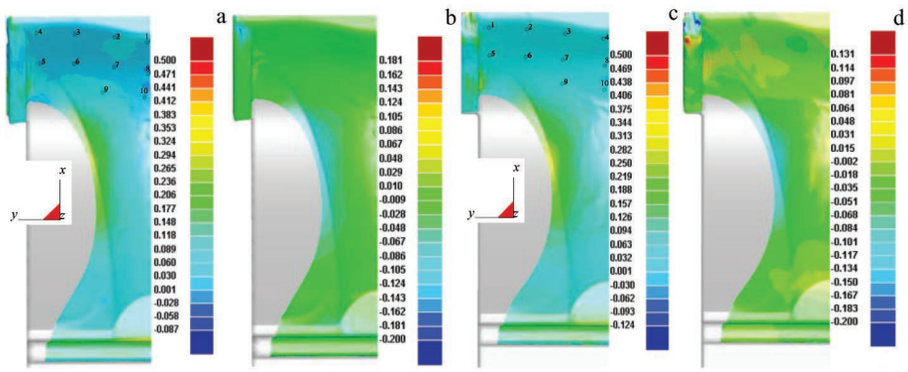

Fig.16 Predicted major strain ε_1 (a, c) and minor strain ε_2 (b, d) distributions of saddle shape parts with Drawbead C (a, b) and Drawbead E (c, d) under Hill 48 yield criterion

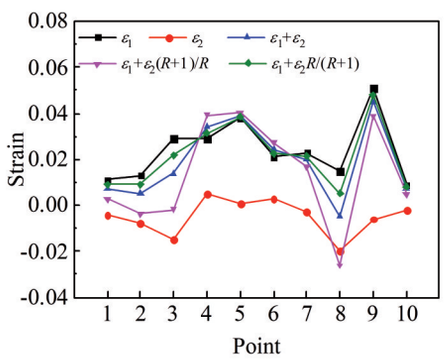

Fig.17 Strains at selected 10 points of saddle shape parts with Drawbead E under Hill 48 yield criterion

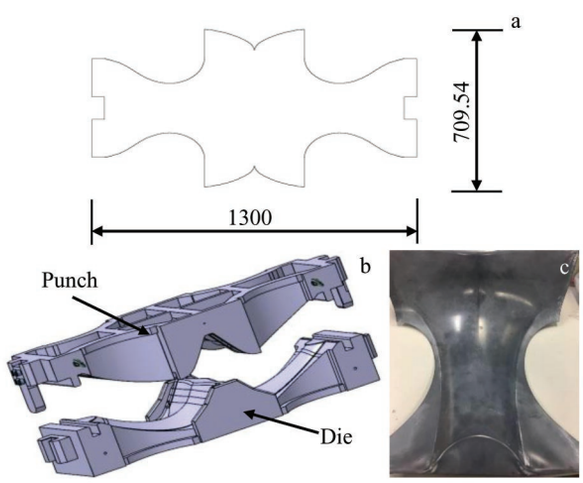

Fig.18 Schematic diagrams of blank (a) and hot stamping tools (b); appearance of saddle shape part (c)

$$S_d = \frac{1}{n-1}\sum_{i=1}^{n}\left[T_i - \frac{1}{n}\left(\sum_{i=1}^{n} T_i\right)\right]^2 \quad (21)$$

$$R_e = \frac{1}{n}\sum_{i=1}^{n}\frac{|T_{ei} - T_{si}|}{T_{ei}} \times 100\% \quad (22)$$

where T_{max} is the maximum thickness, T_i is the measured thickness at Point i, T_{min} is the minimum thickness, n is the number of the measured points, T is the blank thickness (0.8 mm), T_{ei} is the experiment thickness, and T_{si} is the simulation thickness.

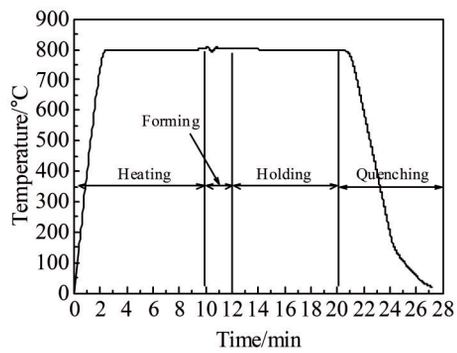

Fig.19 Heating path of blank during hot stamping

The calculated R_{max}, T_a, R_{min}, S_d, and R_e of the experiment and simulation results are shown in Table 4. The simulation results of R_{max} and T_a with different yield criteria are close to each other, but smaller than the experiment results. The relative error of the simulation based on Barlat 89 yield criterion is slightly smaller.

4.2 Microstructure

The microstructures of the initial sheet and the formed part are shown in Fig.21. The microstructure of the drawbead area in the formed saddle shape part is shown in Fig. 22. The volume fraction of α and β phases are presented in Fig.23. It is clear that the microstructures of the initial sheet and the formed saddle shape part are composed of equiaxed α phase and intergranular β phase. After hot stamping, the volume fraction of β phase increases by about 9.63vol%, compared with that of the initial sheet, inferring the obvious phase transformation. The microstructure evolution is mainly the grain growth and phase transformation in the drawbead area. The hardness of the initial sheet and the formed saddle shape part is 3949.4 and 4106.2 MPa, respectively. It can be seen that the hardness of the formed saddle shape part increases slightly.

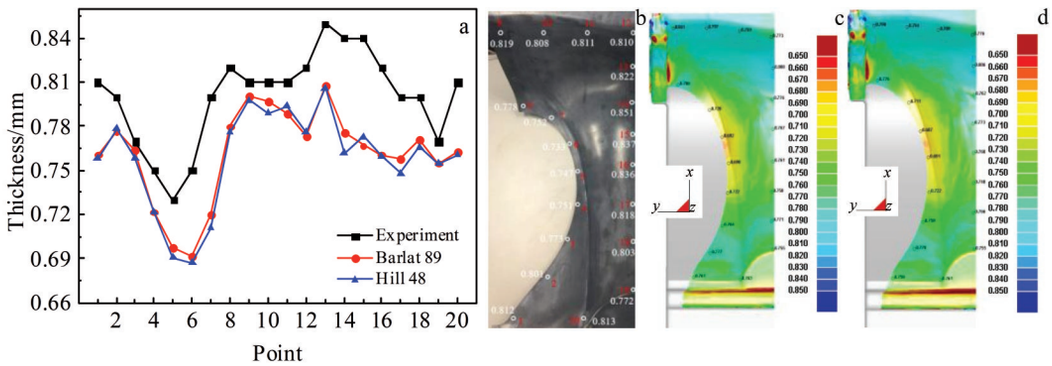

Fig.20 Thickness distributions of experiment and simulation results: (a) thickness of 1~20 points; (b) experimental results of thickness; (c) simulation results with Barlat 89 yield criterion of thickness; (d) simulation results with Hill 48 yield criterion of thickness

Table 4 Experiment and simulation results of R_{max}, T_a, R_{min}, S_d and R_e

Parameter	R_{max}/%	T_a/mm	R_{min}/%	S_d	R_e/%
Experiment	6.25	0.800 50	8.750	0.001 005	-
Simulation with Barlat 89	1.00	0.761 65	13.500	0.001 029	4.827 179
Simulation with Hill 48	0.75	0.758 50	14.125	0.001 088	5.224 155

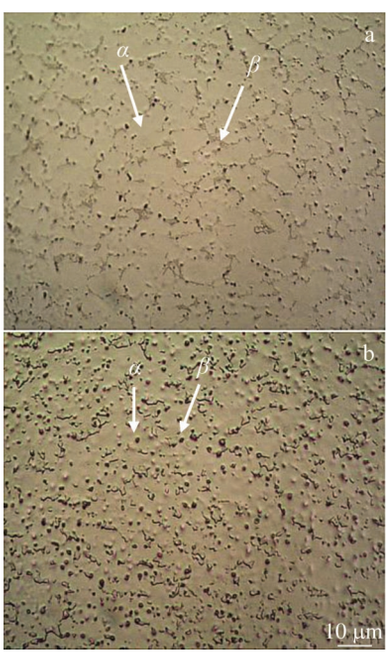

Fig.21 Microstructures of initial TA32 alloy sheet (a) and formed saddle shape part (b)

4.3 Mechanical properties

After hot stamping, the tensile specimens were cut from the formed saddle shape parts to verify the mechanical properties. The true stress-true strain curves of the initial sheet and the formed saddle shape part room temperature are shown in Fig. 24. After hot stamping, the elongation reduces from 10.1% to 6.67%, and the tensile strength reduces from 1359 MPa to 1276 MPa. This is because the reduction in equiaxed α phase and the increase in grain size lead to a lower chaotic level of the cluster domain direction. Thus, the obstruction against dislocation motion is reduced, resulting in the decrease of strength and elongation.

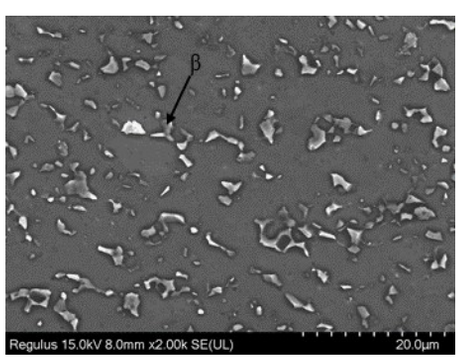

Fig.22 Microstructure of drawbead area in formed saddle shape part

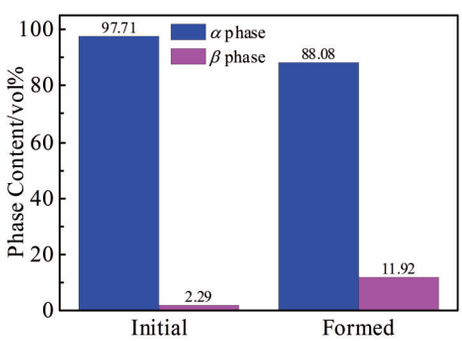

Fig.23 Volume fractions of α and β phases of initial TA32 alloy sheet and formed saddle shape part

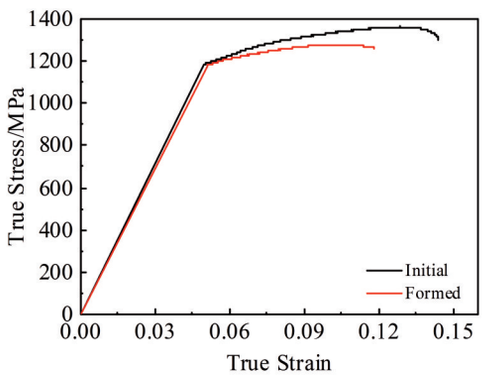

Fig. 24 True stress-true strain curves of initial TA32 alloy sheet and formed saddle shape part

5 Conclusions

1) The addition of drawbeads along *X* and *Y* axes can increase the major strain and the minor strain by restricting the stress flow into the middle part of the saddle shape part, therefore reducing the wrinkle risk. The drawbeads can effectively eliminate the wrinkles of saddle shape parts.

2) The finite element models based on Barlat 89 and Hill 48 yield criteria have the similar prediction accuracy for the thickness distribution. The simulated thickness is lower than the experiment one. The finite element models based on Barlat 89 yield criterion is better for the numerical simulation of the hot stamping of TA32 alloy.

3) The hot stamping process has slight effects on mechanical properties and microstructure of TA32 alloy saddle shape part.

References

1 Banerjee D, Williams J C. *Acta Materialia*[J], 2013, 61(3): 844

2 Singh P, Pungotra H, Kalsi N S. *Materials Today: Proceedings* [J], 2017, 4(8): 8971

3 Cheng Chao, Chen Zhiyong, Li Hongen *et al*. *Materials Science and Engineering A*[J], 2021, 800: 140 362

4 Fan R, Yong W U, Chen M *et al*. *Transactions of Nonferrous Metals Society of China*[J], 2020, 30(4): 928

5 Liu Zhangguang, Li Peijie, Yin Xiyue *et al*. *Rare Metal Materials and Engineering*[J], 2018, 47(11): 3473 (in Chinese)

6 Ma B L, Wu X D, Li X J *et al*. *Materials & Design*[J], 2016, 94: 9

7 Wang K H, Kopec M, Chang S P *et al*. *Materials & Design*[J], 2020, 194: 108 948

8 Chen C, Chen M H, Xie L S *et al*. *The International Journal of Advanced Manufacturing Technology*[J], 2019, 103(1-4): 807

9 Wu Ronghua, Chen Minghe, Xie Lansheng *et al*. *Rare Metal Materials and Engineering*[J], 2019, 48(10): 3142 (in Chinese)

10 Gantar G, Pepelnjak T, Kuzman K. *Journal of Materials Processing Technology*[J], 2002, 130-131: 54

11 Naceur H, Guo Y Q, Batoz J L *et al*. *International Journal of Mechanical Sciences*[J], 2001, 43(10): 2407

12 Colgan M, Monaghan J. *Journal of Materials Processing Technology*[J], 2003, 132(1-3): 35

13 Grechnikov F, Khaimovich A, Alexandrov S. *Journal of Materials Processing Technology*[J], 2016, 234: 300

14 Wang X, Cao J. *International Journal of Mechanical Sciences* [J], 2000, 42(12): 2369

15 Hajari A, Morakabati M, Abbasi S M *et al*. *Materials Science and Engineering A*[J], 2017, 681: 103

16 Kotkunde N, Deole A D, Gupta A K *et al*. *Materials & Design* [J], 2014, 55: 999

17 Kim J B, Yang D Y, Yoon J W *et al*. *International Journal of Plasticity*[J], 2000, 16(6): 649

18 Kotkunde N, Deole A D, Gupta A K *et al*. *Materials & Design* [J], 2014, 63: 336

19 Neto D M, Oliveira M C, Alves J L *et al*. *Materials & Design*[J], 2014, 60: 368

20 Kotkunde N, Srinivasan S, Krishna G *et al*. *Transactions of Nonferrous Metals Society of China*[J], 2016, 26(3): 736

21 Liu Zhangguang, Li Peijie, Geng Linlin *et al*. *Materials Science and Engineering A*[J], 2017, 699: 71

22 Chen Can, Chen Minghe, Xie Lansheng *et al*. *Rare Metal Materials and Engineering*[J], 2019, 48(3): 827 (in Chinese)

23 Sudarsan C, Prasad K S, Hazra S *et al*. *Journal of Manufacturing Processes*[J], 2020, 56(A): 1099

24 Vel L, Demazeau G, Etourneau J. *Materials Science Engineering B*[J], 1991, 10(2): 149

25 Fan Ronglei, Chen Minghe, Wu Yong *et al*. *Metals*[J], 2018, 8(12): 985

26 Hill R. *Proceedings of the Royal Society of London Series A*[J], 1948, 193(1033): 281

27 Barlat F, Lian K. *International Journal of Plasticity*[J], 1989, 5(1): 51

TA32钛合金马鞍形零件热冲压工艺数值模拟

宋　飞，王　宁，苏　楠，陈明和，谢兰生
(南京航空航天大学 直升机传动科学与技术国家级重点实验室，江苏 南京 210016)

摘　要：建立了TA32钛合金本构模型，在模具上添加了不同的拉延筋，并对其进行了优化以消除皱纹。使用Barlat 89和Hill 48屈服准则来比较有限元模拟的预测精度。通过热冲压成形实验，测量了TA32钛合金马鞍形零件的厚度分布，并与模拟结果进行比较。结果表明：添加*X*轴和*Y*轴拉延筋可以有效消除皱纹，实现马鞍形零件精确成形，并且无任何缺陷。采用Barlat 89屈服准则的有限元模型比采用Hill 48屈服准则的模型具有更好的预测精度，该有限元模拟具有较好的理论预测意义。研究了成形后零件的力学性能和显微组织，各项性能均达到了实际工程需要。

关键词：TA32钛合金；热冲压；马鞍形零件；有限元模拟；拉延筋；屈服准则

作者简介：宋　飞，男，1992年生，硕士，南京航空航天大学直升机传动科学与技术国家级重点实验室，江苏 南京 210016，E-mail：meefsong@nuaa.edu.cn